

Microwave quantum optics with an artificial atom in one-dimensional open space

Io-Chun Hoi¹, C M Wilson^{1,3}, Göran Johansson¹, Joel Lindkvist¹, Borja Peropadre², Tauno Palomaki¹ and Per Delsing^{1,3}

¹ Department of Microtechnology and Nanoscience (MC2), Chalmers University of Technology, SE-412 96 Göteborg, Sweden

² Instituto de Física Fundamental, CSIC, Calle Serrano 113-bis, Madrid E-28006, Spain

E-mail: per.delsing@chalmers.se and chris.wilson@chalmers.se

New Journal of Physics **15** (2013) 025011 (15pp)

Received 10 October 2012

Published 7 February 2013

Online at <http://www.njp.org/>

doi:10.1088/1367-2630/15/2/025011

Abstract. We address recent advances in microwave quantum optics with artificial atoms in one-dimensional (1D) open space. This field relies on the fact that the coupling between a superconducting artificial atom and propagating microwave photons in a 1D open transmission line can be made strong enough to observe quantum coherent effects, without using any cavity to confine the microwave photons. We investigate the scattering properties in such a system with resonant coherent microwaves. We observe the strong nonlinearity of the artificial atom and under strong driving we observe the Mollow triplet. By applying two resonant tones, we also observe the Autler–Townes splitting. Exploiting these effects, we demonstrate two quantum devices at the single-photon level in the microwave regime: the single-photon router and the photon-number filter. These devices provide important steps toward the realization of an on-chip quantum network.

³ Authors to whom any correspondence should be addressed.



Content from this work may be used under the terms of the [Creative Commons Attribution-NonCommercial-ShareAlike 3.0 licence](https://creativecommons.org/licenses/by-nc-sa/3.0/). Any further distribution of this work must maintain attribution to the author(s) and the title of the work, journal citation and DOI.

Contents

1. Introduction	2
2. Elastic and inelastic scattering	3
3. Mollow triplet and Autler–Townes splitting	7
4. Applications	8
4.1. The single-photon router	8
4.2. The photon-number filter	10
5. Discussion	13
6. Summary	14
Acknowledgments	14
References	14

1. Introduction

During the last decade, circuit QED based on superconducting circuits has become a promising platform to investigate strong coupling between light and matter as well as enable quantum information processing technology [1–3]. Some of the exciting results include the following: strong coupling between a superconducting qubit and a single photon [4], resolving photon-number states [5], synthesizing arbitrary quantum states [6], three-qubit quantum error correction [7], implementation of a Toffoli gate [8], quantum feedback control [9] and architectures for a superconducting quantum computer [10]. The nonlinear properties of Josephson junctions have also been used to study the dynamical Casimir effect [11] and build quantum limited amplifiers [12, 13].

More recently, theoretical and experimental work has begun to investigate the strong interaction between light and a single atom even without a cavity [14–17]. In this system, the destructive interference between the excited dipole radiation and the incident field gives rise to the extinction of the forward propagating wave for a weak incident field. This effect was first demonstrated for a single atom/molecule in three-dimensional space, where the extinction of the forward incident wave did not exceed 12% [14, 16]. This is due to the spatial mode mismatch between the incident and scattered waves.

However, by taking advantage of the confinement of the propagating fields in a one-dimensional (1D) open transmission line and the huge dipole moment of an artificial atom [18–25], strong coupling between an artificial atom and a propagating field can be achieved. Extinctions in excess of 99% have been observed [19, 20]. This system represents a potential key component in the field of microwave quantum optics, which is the central scope of this paper.

This paper is organized as follows. The elastic and inelastic scattering properties of the single artificial atom are presented in section 2. Well-known quantum optics effects, such as the Mollow triplet and Autler–Townes splitting (ATS), are presented in section 3. In section 4, we demonstrate two quantum devices based on these effects which operate at the single-photon level in the microwave regime, namely the single-photon router and the photon-number filter. In section 5, we discuss the possibilities of a quantum network using these devices.

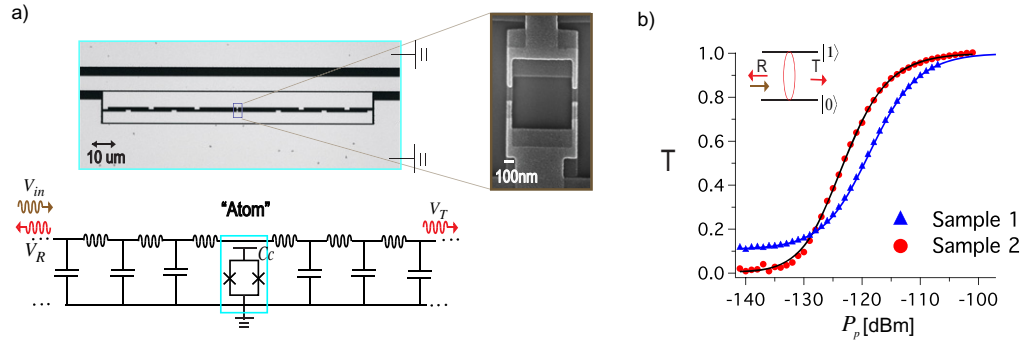


Figure 1. (a) Top: a micrograph of the artificial atom, a superconducting transmon qubit embedded in a 1D open transmission line. (Magnified section) Scanning-electron micrograph of the superconducting quantum interference device (SQUID) loop of the transmon. Bottom: the corresponding circuit model. (b) Measured transmittance, $T = |t|^2$, on resonance as a function of the incoming probe power, P_p , for samples 1 and 2. At low power, very little is transmitted whereas at high power T approaches unity. (Inset) A weak, resonant coherent field is reflected by the atom.

2. Elastic and inelastic scattering

In figure 1(a), a transmon qubit [26] is embedded in a 1D open transmission line with a characteristic impedance $Z_0 \simeq 50 \Omega$. The 0–1 transition energy of the transmon, $\hbar\omega_{10}(\Phi) \approx \sqrt{8E_J(\Phi)E_C} - E_C$, is determined by two energies, where $E_C = e^2/2C_\Sigma$ is the charging energy, C_Σ is the total capacitance of the transmon, $E_J(\Phi) = E_J|\cos(\pi\Phi/\Phi_0)|$ is the Josephson energy which can be tuned by the external flux Φ , E_J is the maximum Josephson energy and $\Phi_0 = h/2e$ is the magnetic flux quantum.

With a coherent state input, we investigate the transmission and reflection properties of the field. The input field, transmitted field and reflected field are denoted as V_{in} , V_T and V_R , respectively, indicated in the bottom panel of figure 1(a). The reflection coefficient, r , can be expressed as [18]

$$r = \frac{V_R}{V_{in}} = -r_0 \frac{1 - i\delta\omega_p/\gamma_{10}}{1 + (\delta\omega_p/\gamma_{10})^2 + \Omega_p^2/(\Gamma_{10} + \Gamma_l)\gamma_{10}}, \quad (1)$$

where the maximum reflection amplitude is given by $r_0 = \Gamma_{10}/2\gamma_{10}$. Γ_{10} is the relaxation rate of the 0–1 transition of the atom. $\gamma_{10} = \Gamma_{10}/2 + \Gamma_{\phi,l}$ is the 0–1 decoherence rate and $\delta\omega_p = \omega_p - \omega_{10}$ is the detuning between the applied probe frequency, ω_p , and the 0–1 transition frequency, ω_{10} . $\Gamma_{\phi,l} = \Gamma_\phi + \Gamma_l/2$, where $\Gamma_{\phi,l}$ is the sum of the non-radiative rates, i.e. the intrinsic losses, Γ_l and the pure dephasing rate, Γ_ϕ . We see that both r_0 and γ_{10} are uniquely dependent on $\Gamma_{\phi,l}$ and Γ_{10} . Ω_p is the Rabi oscillation frequency induced by the probe, which is proportional to V_{in} [26],

$$\Omega_p = \frac{2e}{\hbar} \frac{C_c}{C_\Sigma} \left(\frac{E_J}{8E_C} \right)^{1/4} \sqrt{P_p Z_0}, \quad (2)$$

where $P_p = |V_{in}|^2/2Z_0$ is the probe power. By definition, the transmission coefficient $t = V_T/V_{in} = 1 + r$. The level of V_{in} is assumed to be the same as the off resonance value. The

relaxation process is dominated by coupling to the 1D transmission line through the coupling capacitance C_c (see the bottom panel of figure 1(a)) and assuming that photon emission to the transmission line dominates the relaxation, we find that $\Gamma_{10} \simeq \omega_{10}^2 C_c^2 Z_0 / (2C_\Sigma)$. This relaxation originates from coupling to a continuum of modes, as opposed to the cavity case, where the artificial atom is coupled solely to a single mode.

According to equation (1), for a weak ($\Omega_p \ll \gamma_{10}$) resonant probe ($\delta\omega_p = 0$), in the absence of both pure dephasing ($\Gamma_\phi = 0$) and non-radiative decay ($\Gamma_l = 0$), we should see full reflection ($|r| = 1$) of the incoming probe field [24, 25, 27]. In that case, we also have full extinction, $|t| = 0$, of the propagating wave. This full extinction (perfect reflection) can be described as a coherent interference of the incoming wave and the scattered wave from the atom. This is what we observe in figure 1(b), where we measure the transmittance, $T = |t|^2$, on resonance as a function of P_p with two samples. We see an extinction in the resonant microwaves of up to 90% (99%) for sample 1 (2) at low incident probe power, where $\Omega_p \ll \gamma_{10}$. For increasing P_p , we see the strong nonlinearity of the atom which becomes saturated by the incident microwave photons. Since the atom can only scatter one photon at a time, at high incident power, $\Omega_p \gg \gamma_{10}$, most of the photons pass the atom without interaction and are thus transmitted. Therefore $|t|$ tends toward unity for increasing P_p , consistent with equation (1). We define the average probe photon number coming to the transmon per interaction time as $\langle N_p \rangle = P_p / (\hbar\omega_p(\Gamma_{10}/2\pi))$.

We measure t as a function of P_p and ω_p . In figure 2, the experimental magnitude, $|t|$, and phase response, φ_p , for sample 1 are shown in panels (a), (b), respectively. The top and bottom panels display two-dimensional plots and the corresponding line cuts indicated by the arrows, respectively. For $\langle N_p \rangle \ll 1$, the magnitude response shows a strong extinction of resonant microwaves, up to 70% in amplitude or $\sim 90\%$ in power (figure 1(b)). The solid curves of figure 2 show fits to all magnitude and phase curves simultaneously, with three fitting parameters, $\Gamma_{10}/2\pi = 73$ MHz, $\Gamma_{\phi,1}/2\pi = 18$ MHz and $\omega_{10}/2\pi = 7.1$ GHz. This corresponds to $C_c = 25$ fF, $\gamma_{10}/2\pi = 55$ MHz and $r_0 = 0.67$. We find very good agreement between theory and experiment. We also see that r varies as a function of P_p and ω_p , as expected (data not shown).

In order to measure the resonant scattered field, V_R , from the atom, we need to cancel background reflections and circulator leakage in the setup. In figure 3(a), after splitting the input field, the phase and amplitude in one arm are varied such that the field through a directional coupler destructively interferes with the coherent leakage from the circulator and background reflections (see green curves). We send a pulse at ω_{10} and measure the scattered (reflected) fields from the artificial atom. We use a phase-sensitive average $\langle V_R \rangle^2$ to capture the elastic (coherent) component of the scattered field. For the total scattered field, the sum of the elastically and inelastically scattered fields, we use a phase-insensitive average $\langle V_R^2 \rangle$. By pulsing the input, we are able to subtract amplifier noise from our measurement of the total scattered field.

In figure 3(b), we show $\langle V_R^2 \rangle$ and $\langle V_R \rangle^2$ as a function of resonant incident power for two different measurement bandwidths (BW). We see that the amount of the inelastic field that we capture depends on the BW. The solid curves are theory fits using the model in figure 3(c) (integrating the Mollow triplet), with the parameters in table 1, sample 2. As expected, at low incident power, we see the $\langle V_R \rangle^2 \simeq \langle V_R^2 \rangle \simeq \langle V_{in}^2 \rangle$. This suggests that both the dephasing and non-radiative decay are small, and not resolvable from the data. At high incident fields, where $\Omega_p > \Gamma_{10}$, the main contribution to the total field is from inelastic scattering. The power associated with intrinsic losses is $P_l = P_p - P_R - P_T$, where P_R , P_T are the total power reflected and transmitted, respectively. For a resonant probe, we can estimate the loss rate Γ_l using the

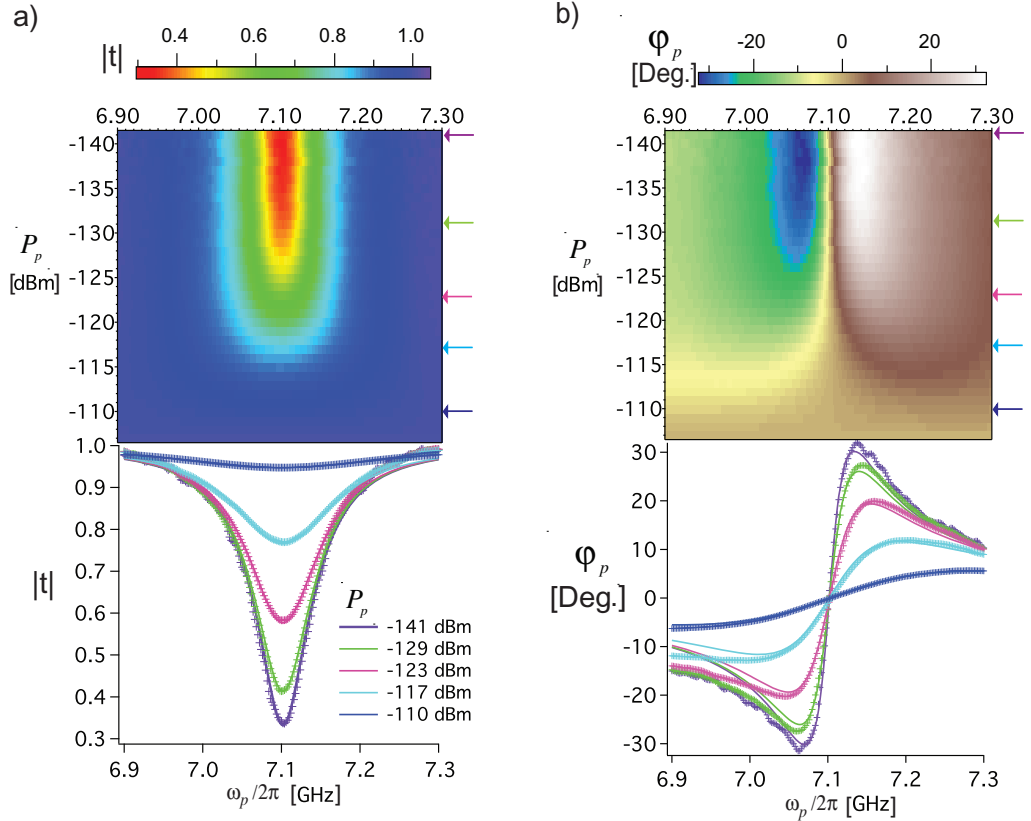


Figure 2. t as a function of P_p and ω_p (sample 1). (a) The magnitude response; (b) the phase response. Top panel: experimental data. Bottom panel: we show the line cuts for five different powers, as indicated by the arrows on the top panel. The experimental data (markers) are fit simultaneously using equation (1) (curves). The magnitude response demonstrates a strong coupling between the atom and resonant propagating microwaves, whereas the phase response shows anomalous dispersion [18].

following expression:

$$P_l = \hbar\omega_{10}\rho_{11}\Gamma_l = \frac{2r_0\Gamma_l/(\Gamma_{10} + \Gamma_l)}{1 + \Omega_p^2/(\Gamma_{10} + \Gamma_l)\gamma_{10}} P_p,$$

where ρ_{11} is the probability for the atom to be in the first excited state. We do not have sufficiently accurate data to extract the loss rate for these measurements. We can, however, set an upper limit on the loss rate. For sample 2, $\Gamma_{\phi,l}/2\pi \simeq 1.1$ MHz, which means that $\Gamma_l/2\pi$ is less than 2.2 MHz.

To further characterize sample 1, the frequency of the resonance dip in transmission in figure 2(a) is mapped as a function of Φ with a weak probe, $\Omega_p \ll \gamma_{10}$ (see figure 4(a)), in the transmon regime, where $E_J/E_C \geq 20$, $\delta\omega_p \approx \omega_p - [\sqrt{8E_J}|\cos(\pi\Phi/\Phi_0)|E_C - E_C]/\hbar$. If we increase P_p to a level such that the 0–1 transition is saturated, two-photon (0–2) transitions occur, as indicated by the gray curve of figure 4(b). The transition frequency corresponds to $(\omega_{10} + \omega_{21})/2$, where ω_{21} is the 1–2 transition energy. We use a Cooper pair box [26] Hamiltonian with 50 charge states to fit the spectrum of the atom and extract $E_J = 12.7$ GHz,

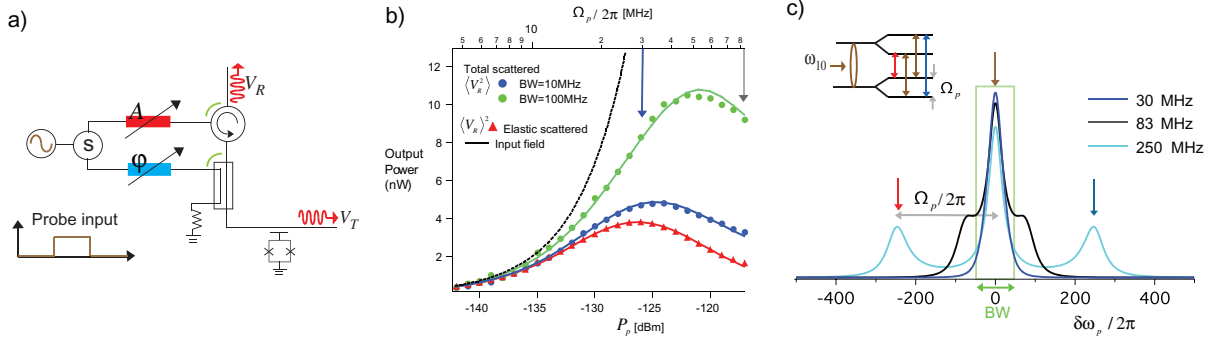


Figure 3. Elastic versus inelastic scattering from the artificial atom (sample 2). (a) Measurement setup, with calibration of background reflection, i.e. leakage from the circulator. The green curves represent the leakage fields from the circulator and the fields through the directional coupler. By tuning the phase (blue box) and attenuation (red box), these two fields can cancel each other. (b) The coherently/elastically reflected power (phase-sensitive average, red curve) or total reflected power (phase-insensitive average, green and blue curves) as a function of resonant P_p for different BW. The total power reflected is the sum of both the elastic and inelastic fields. Solid curves are the theory fits to experimental data, with extracted parameters of table 1. The black curve shows the input power for comparison. At low powers, $\langle N_p \rangle \ll 1$, we observed that $\langle V_R \rangle^2 \simeq \langle V_R^2 \rangle \simeq \langle V_{in}^2 \rangle$. At high powers, $\langle N_p \rangle > 1$, more and more photons are inelastically scattered as the Mollow triplet begins to emerge. The wider the BW, the more of the Mollow triplet we capture. Note that the output power includes the 79 dB gain of the amplifiers. (c) Theory plot for the situation when a microwave pump is applied at ω_{10} . As the power of the ω_{10} pump increases, the Mollow triplet appears in the spectrum with peak separation equal to the Rabi frequency Ω_p . (Inset) Dressed state picture of the energy levels.

Table 1. Parameters for samples 1–3. All values are in GHz (except for the extinction and E_J/E_C).

Sample	E_J/h	E_C/h	E_J/E_C	$\omega_{10}/2\pi$	$\omega_{21}/2\pi$	$\Gamma_{10}/2\pi$	$\Gamma_{\phi,1}/2\pi$	Extinction (%)
1	12.7	0.59	21.6	7.1	6.38	0.073	0.018	90
2	10.7	0.35	31	5.13	4.74	0.041	0.0011	99
3	—	—	—	4.88	4.12	0.017	0.0085	75

$E_C = 590$ MHz for sample 1. The extracted parameters are summarized in table 1. Note that one of the Josephson junctions is broken in sample 3; therefore, the transition frequency could not be tuned with Φ .

The extinction efficiency of sample 2 is much better than that of sample 1. This is because sample 1 has a low $E_J/E_C \sim 21.6$, which is barely in the transmon limit. For this value of E_J/E_C , charge noise still plays an important role as the energy band of the 0–1 transition is still dependent on charge [26]. For sample 1, we find that the charge dispersion is 7 MHz and the dephasing is dominated by charge noise. By increasing E_J/E_C to 31, we see much less dephasing in sample 2, which gives nearly perfect extinction of propagating resonant

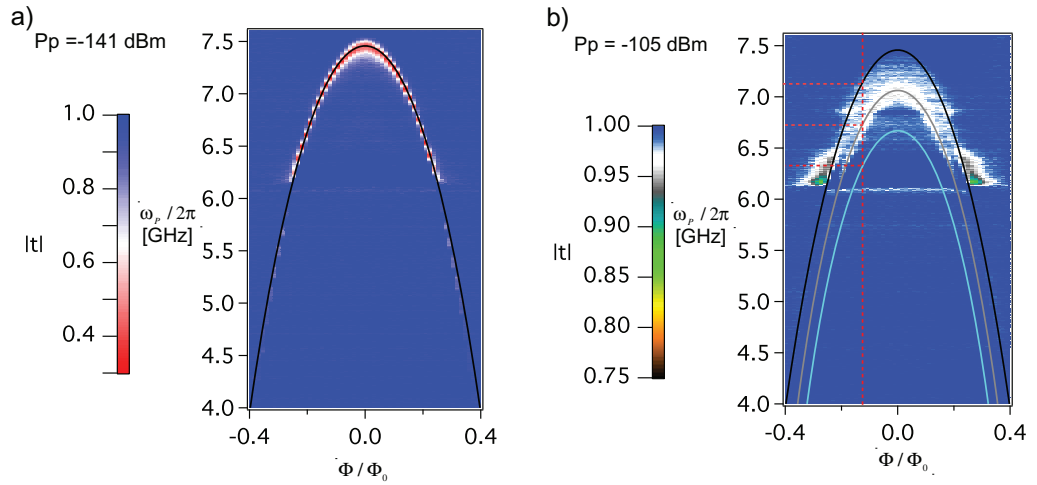


Figure 4. $|t|$ as a function of Φ for sample 1. (a) At weak probe power, where $\Omega_p \ll \gamma_{10}$. The black curve is the theory fit to the 0–1 transition. (b) At high probe power, where $\Omega_p \gg \gamma_{10}$. The black and blue curves correspond to the 0–1 and 1–2 transitions, respectively. The gray curve is the two-photon (0–2) transition. The red dashed line indicates the flux bias point and the corresponding ω_{10} , $\omega_{20}/2$, ω_{21} for figure 2 and figures 5(a), (c) and (d). There is a stray resonance around 6.1 GHz.

microwaves. Note that the anharmonicity between ω_{10} and ω_{21} of sample 2 is close to E_C . This is not quite the case for sample 1 due to its low E_J/E_C [26].

3. Mollow triplet and Autler–Townes splitting

As shown in the previous section, the transmon also has higher level transitions; in particular, we are interested in the 1–2 transition with frequency ω_{21} . By using two-tone spectroscopy, the ω_{21} transition can be directly measured. We can saturate the ω_{10} transition by applying a pump field at $\omega_{10} = 7.1$ GHz, and measure the transmission properties using a weak probe ω_p . As the pump power is increased, the population of the first excited state increases; therefore, we start observing photon scattering from the 1–2 transition, which appears as a dip in transmission at $\omega_p = \omega_{21}$, see figure 5(a). The dip in transmission grows until the 0–1 transition becomes fully saturated. From this, we extract $\omega_{21}/2\pi = 6.38$ GHz for sample 1. Therefore, the two-photon (0–2) transition should be equal to 6.74 GHz, consistent with the observation in figure 4(b). The linewidth of ω_{21} is around 120 MHz; this dephasing mainly comes from the charge dispersion. Further increasing the pump power at ω_{10} , we observe the well-known Mollow triplet [18, 28] (figure 5(b), sample 3). The Rabi splitting of the triplet can be used to calibrate the power at the atom. The Mollow triplet can be explained in the dressed state picture, where the two lowest levels are split by the Rabi frequency. These four states give three different transitions, indicated by red, brown and blue arrows in the inset of figure 5(b), consistent with figure 3(c). Note that the way we observed the triplet here is different from that in [18]. We probe the transmission of these triplet transitions instead of looking at the emission spectrum. We see that the center transition is much less visible, because we pump at the frequency which saturates the transition.

With a weak resonant probe field, $\Omega_p \ll \gamma_{10}$, $\omega_p = \omega_{10}$, and a strong resonant, $\omega_c = \omega_{21}$, control field, the 0–1 resonance dip splits with the magnitude of Ω_c [22]; this is known as the

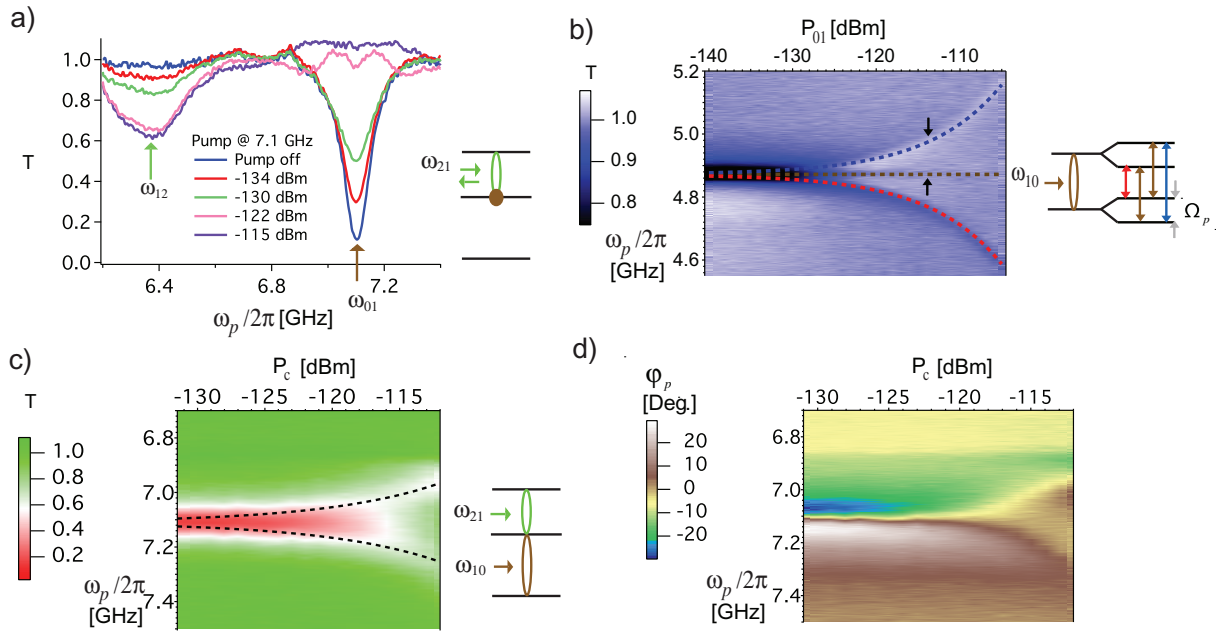


Figure 5. Two-tone spectroscopy. (a) As the frequency of a weak probe field is swept, a second microwave drive is continuously applied at ω_{10} with increasing powers. We see that another dip gradually appears in the probe transmission response. (b) T as a function of the probe frequency and pump power. As the power of ω_{10} further increases, we see the Mollow triplet. The dashed lines indicate the calculated position of the triplet. (Inset) Schematic picture of triplet transitions in the dressed state picture. Note that we use sample 3, where $\omega_{10}/2\pi = 4.88$ GHz. (c) A second microwave drive is applied at ω_{21} with variable power, P_c . Magnitude response in (c). As P_c increases, we see induced transmission at $\omega_p = \omega_{10}$. With a strong drive applied, the ATS appears with the magnitude of $\Omega_c/2\pi$ (black dashed lines). (d) Phase response of the probe.

ATS [29]. The magnitude and phase response are shown in figures 5(c) and (d), respectively. In the magnitude response, we see that the transmon becomes transparent for the probe at $\omega_p = \omega_{10}$ at sufficiently high control power. In the phase response, we see that the probe phase, φ_p , depends on the control power, P_c .

In the following section, we demonstrate two devices based on these effects which could be utilized in a microwave quantum network. By making use of the ATS, we demonstrate a router for single photons. By using the high nonlinearity of the atom, we demonstrate a photon-number filter, where we convert classical coherent microwaves into a non-classical microwave field.

4. Applications

4.1. The single-photon router

The operation principle of the single-photon router is explained as follows. In the time domain (see figure 6(a)), we input a constant weak probe in the single-photon regime, $\langle N_p \rangle \ll 1$, at $\omega_p = \omega_{10}$. We then apply a strong control pulse, around 30 dB more than the probe power, at

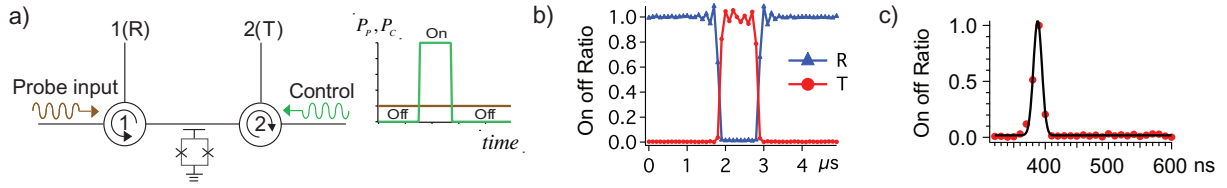


Figure 6. The single-photon router, data for sample 2. (a) Measurement setup and the control pulse sequence. A strong control pulse at $\omega_c = \omega_{21}$ is used to route a weak continuous microwave $\omega_p = \omega_{10}$. Depending on whether the control pulse is on or off, the probe field is delivered to output port 2 or 1, respectively. (b), (c) Normalized on–off ratio (see text) of the transmittance (T) and reflectance (R) of ω_p measured simultaneously. (b) The control pulse is shaped as a square pulse with 1 μ s duration. (c) A Gaussian pulse with a duration of 10 ns; we see up to 99% on–off ratio. The black curve in panel (c) is a Gaussian fit to the data.

the ω_{21} frequency. When the control is off, the probe photons are reflected by the atom, and delivered to output port 1. When the control is on, the probe photons are transmitted based on ATS and delivered to output port 2. We measure the reflected and the transmitted probe power simultaneously in the time domain. It is crucial to investigate if the microwave photon transport is a fully coherent process, i.e. the transmission dip seen in figure 2(a) is because the photons are being reflected (not due to dissipation). Note that the measurement quantity is phase sensitive, since we measure $\langle V \rangle^2$ rather than $\langle V^2 \rangle$; this means that $\langle V \rangle^2$ is only sensitive to the coherent part of the signal. The experimental setup is shown in figure 6(a).

The results are shown in figures 6(b) and (c) with two different control pulses for sample 2. In figures 6(b) and (c), we use a square (Gaussian) control pulse with a duration of 1 μ s (10 ns). As expected, when the control signal is on, the probe power of the transmitted signal is increased and we see a corresponding decrease in the reflected probe signal. A 99% probe on–off ratio is achieved in both reflection and transmission for sample 2. We also see that the on–off ratio does not depend on the control time. In figure 6(c), the time resolution of our digitizer detector/arbitrary waveform generator is 5 ns, which prevents us from accurately measuring pulses less than about 10 ns. The ringing signals appearing in figure 6(b) are artifacts of the digitizer. In the setup of figure 6(a), we send ω_{10} and ω_{21} in opposite directions with respect to each other. We can also send pulses in the same direction by using a microwave combiner at one of the input ports and get the same results, as expected. Note that we use the on–off ratio $[R(\Omega_c) + R_b]/[R(0) + R_b]$ [19], where $R(\Omega_c)$ and $R(0)$ represent reflectance when the control is on and off, respectively, and R_b accounts for background reflections in the line and leakage through circulator 1 (figure 6(a)). We note that these data were taken without canceling the leakage as shown in figure 3. For the on–off ratio of the transmittance $T(0)/T(\Omega_c)$, we can calibrate the transmittance, $T(0) = [T(0)/T(\Omega_c)]T_{\text{VNA}}(\Omega_c)$, where $T_{\text{VNA}}(\Omega_c) \simeq 98.4\%$ is the transmittance on resonance with the corresponding P_c in figure 5(c). $T(\Omega_c)$ and $T(0)$ represent the transmittance when the control is on and off, respectively. Theoretically, for sample 2, when the control signal is off, we have $R(0) = |\Gamma_{10}/2\gamma_{10}|^2 \simeq 91\%$, $T(0) = |1 - \Gamma_{10}/2\gamma_{10}|^2 \simeq 0.2\%$ and $D_{\phi,l}(0) \simeq 8.8\%$. When the control signal is on, we have $R(\Omega_c) \simeq 0$, $T(\Omega_c) \simeq 1$ and $D_{\phi,l}(\Omega_c) \simeq 0$, where $D_{\phi,l}$ refers to the total dissipation associated with intrinsic losses and pure dephasing.

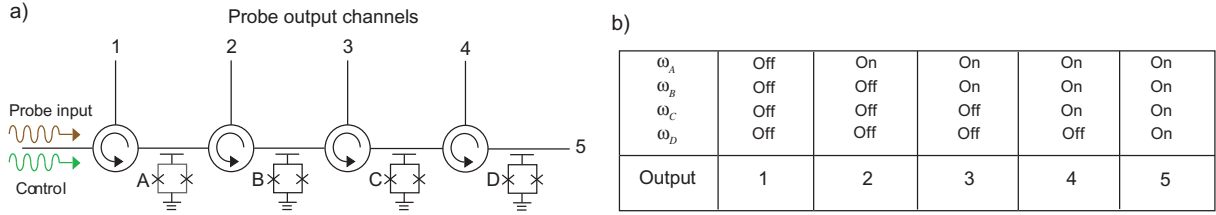


Figure 7. A multiport router. (a) Cartoon of a multiport router: single-photon routers cascaded to many output channels. Here we show a five-port router using four atoms (A–D) in series, each separated by a circulator. The ω_{10} of the atoms are the same, whereas the 1–2 transition frequencies, $\omega_{21,A} \neq \omega_{21,B} \neq \omega_{21,C} \neq \omega_{21,D}$, are different. By turning on and off control tones at the various 1–2 transition frequencies, we can determine the output channel of the probe field, according to the table in (b).

The speed of our router sample 1 (2) is predicted to be $1/\Gamma_{10} \sim 2$ ns (4 ns). We show that the router works well down to the time limit of our instruments. By engineering the relaxation rate, it should be possible to achieve even faster switching times in the sub-nanosecond regime. In addition, the routing efficiency, $R = |r_0|^2$, can be improved by further reducing Γ_ϕ . An improvement in sample 2 compared with sample 1 was achieved by increasing the E_J/E_C ratio. This reduced the sensitivity to the charge noise and therefore the dephasing.

Our router can also be easily cascaded to distribute photons to many output channels. Figure 7(a) shows four atoms (A–D) in series, each separated by a circulator. The ω_{10} of the atoms are the same, whereas the ω_{21} are different. This arrangement can be designed in a straightforward manner by controlling the ratio of E_J/E_C . By turning on and off control tones at the various 1–2 transition frequencies of different atoms, we can determine the output channel of the probe field, according to the table of figure 7(b). For instance, if we want to send the probe field to channel 4, we apply three control tones at $\omega_{21,A}$, $\omega_{21,B}$, $\omega_{21,C}$. Note that regardless of the number of output channels, all the control tones and the probe tone can be sent through the same input port. Theoretically, the maximum number of output channels depends on the ratio of the anharmonicity and the width of the 1–2 transition, γ_{21} . Thus, there is a tradeoff between efficiency and the number of outputs.

4.2. The photon-number filter

In figure 1(b), we demonstrated the nonlinear nature of the artificial atom. This naturally comes from the fact that atoms can only reflect one photon at a time. To reveal the non-classical character of the reflected field, we investigate its statistics. In particular, in this section, we show that the reflected field is antibunched [25]. In addition, we also show that the transmitted field is superbunched [25].

The incident coherent state can be written in terms of a superposition of photon number states, with a Poissonian distribution. For a weak probe field with $\langle N_p \rangle < 0.5$, this coherent field can be approximated using the basis of the first three-photon number states. For a one-photon incident state, the atom reflects it, leading to antibunching in the reflected field. Together with the zero-photon state, the reflected field still maintains first-order coherence, as there is a well-defined phase between the zero- and one-photon states. Because the atom is not able to scatter

more than one photon at a time, a two-photon incident state has a much higher probability of transmission, leading to superbunching in the transmitted field [25, 30]. In this sense, our single artificial atom acts as a photon-number filter, which filters and reflects the one-photon number state from a coherent state. This process leads to a photon-number redistribution between the reflected and transmitted fields [30].

A schematic illustration of the measurement setup is shown in figure 8(a). This allows us to measure the Hanbury Brown–Twiss [31] type power–power correlations. We apply a resonant coherent microwave field at $\omega_p = \omega_{10}$. Depending on whether we send the input through circulator 1 or 2, we measure the statistics of the reflected or transmitted field, respectively. The signal then propagates to a beam splitter, which in the microwave domain is realized by a hybrid coupler, where the outputs of the beam splitter are connected to two nominally identical high electron mobility transistor (HEMT) amplifiers with system noise temperatures of approximately 7 K. We assume that the amplifier noise generated in the two independent detection chains is uncorrelated. After further amplification, the two voltage amplitudes of the outputs are captured by a pair of vector digitizers.

The second-order correlation function [32] provides a statistical tool to characterize the field; it can be expressed as

$$g^{(2)}(\tau) = 1 + \frac{\langle \Delta P_1(t) \Delta P_2(t + \tau) \rangle}{[\langle P_1(t) \rangle - \langle P_{1,N}(t) \rangle][\langle P_2(t) \rangle - \langle P_{2,N}(t) \rangle]},$$

where τ is the delay time between the two digitizers, and P_1 and P_2 are the output powers in ports 1 and 2, respectively, see figure 8(a). $P_{1,N}$, and $P_{2,N}$ are the amplifier noise in ports 1 and 2, respectively, when the incident source is off. Therefore, $[\langle P_i(t) \rangle - \langle P_{i,N}(t) \rangle]$ represents the net power of the field from output port i , where $i = 1, 2$. $\langle \Delta P_1 \Delta P_2 \rangle$ is the covariance of the output powers in ports 1 and 2, defined as $\langle (P_1 - \langle P_1 \rangle)(P_2 - \langle P_2 \rangle) \rangle$.

We had a trigger jitter of ± 1 sample between the two digitizers. To minimize the effect of this trigger jitter, we oversample and then digitally filter (average) the data in all the $g^{(2)}$ measurements. Here, the sampling frequency is set to 10^8 samples s^{-1} with a digital filter with a bandwidth $BW = 55$ MHz applied to each digitizer for all measurements. For a coherent state, we find that $g^{(2)}(\tau) = 1$ with the qubit detuned from ω_{10} .

In figure 8(b), we plot the measured $g^{(2)}(\tau)$ of the reflected field from our atom. At low powers, where $\langle N_p \rangle \ll 1$, we clearly observe antibunching of the field [25]. The trace here was averaged over 2.4×10^{11} measured quadrature field samples (2 Tbyte of data), computed and averaged over 17 h. We correct the slow drifts, e.g. amplifier gain, every 5 min by switching on and off the incident source. In the future, the measurement efficiency can be significantly improved by incorporating a quantum-limited parametric amplifier [12, 13]. The antibunching behavior at $P_p = -131$ dBm ($\langle N_p \rangle \sim 0.4$), $g^{(2)}(0) = 0.55 \pm 0.04$, reveals the non-classical character of the field. Ideally, we would find that $g^{(2)}(0) = 0$ as the atom can only reflect one photon at a time. The non-zero $g^{(2)}(0)$ we measured originates from four effects: (i) a thermal field at 50 mK temperature, (ii) a finite filter BW, (iii) a trigger jitter between the two digitizers and (iv) stray fields including background reflections in the line and leakage through circulator 1 (figure 8(a)). The complete theory curves include all four non-idealities; the partial theory curves include (i) and (ii), but not (iii) and (iv). The effects of these factors on our measured antibunching are shown in the theory plot figure 8(c). For small BW, within the long sampling time, the atom is able to scatter multiple photons. If $BW \ll \Gamma_{10}, \Omega_p$, the antibunching dip we measure vanishes entirely. This interplay between BW and Ω_p yields a power-dependent $g^{(2)}(0)$,

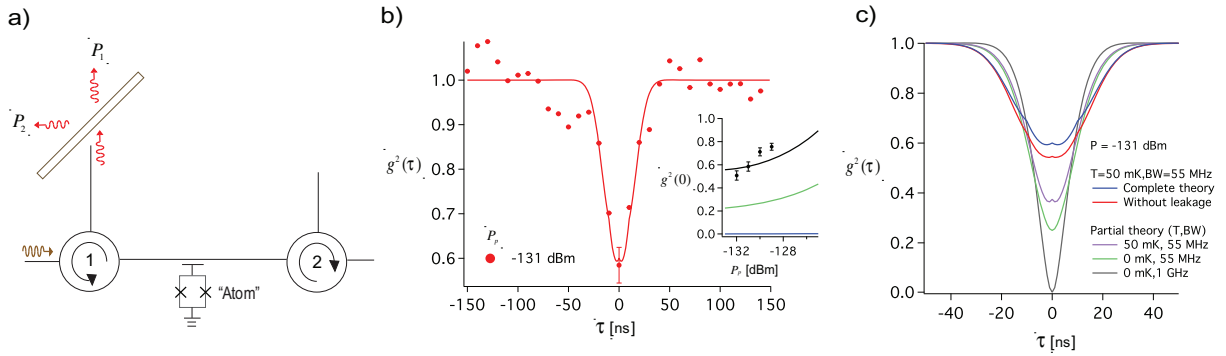


Figure 8. Second-order correlation function of reflected fields generated by the artificial atom (sample 2). (a) A schematic illustration of the physical setup, including circulators (labeled 1, 2) and the hybrid coupler which acts as a beam splitter for the Hanbury Brown–Twiss measurements [31]. Depending on the choice of the input port, we can measure $g^{(2)}$ of the reflected or the transmitted field. (b) $g^{(2)}$ of a resonant reflected field as a function of delay time. We see the antibunched behavior of the reflected field. Inset: $g^{(2)}(0)$ as a function of incident power. The black curve includes all four non-idealities (complete theory) with $BW = 55$ MHz and $T = 50$ mK. The green curve only includes a finite temperature and bandwidth (partial theory) with $T = 50$ mK and $BW = 55$ MHz. The blue curve is the expected result using the partial theory with $BW = 1$ GHz at 0 mK. As the BW decreases or the incident power increases, the degree of antibunching decreases. The error bar indicated for each data (markers) set is the same for all the points. (c) Influence of BW, temperature, leakage and jitter on antibunching. The solid curves in (b) and (c) are the theory curves. For the curves with leakage, we assume that the phase between the leakage field and the field reflected by the atom is 0.37π .

as shown in the inset of figure 8(b). In the ideal case, i.e. for a sufficiently wide BW (1 GHz) at 0 mK, the theory gives $g^{(2)}(0) = 0$, as expected.

In figure 9(a), we see superbunching of the photons [25] with $g^{(2)}(\tau = 0) = 2.31 \pm 0.09 > 2$ at $P_p = -129$ dBm ($\langle N_p \rangle \simeq 0.8$) for the transmitted field. Superbunching occurs because the one-photon state of the incident field has been selectively reflected and thus filtered out from the transmitted signal, whereas the two-photon state is more likely transmitted. The three-photon state and higher number states are negligible. The transmitted state generated from our qubit is thus bunched even more than a thermal state, which has $g_{\text{therm}}^{(2)}(\tau = 0) = 2$. Figure 9(b) shows the theoretical curves of $g^{(2)}(\tau)$ for the transmitted field under the influence of various effects. For the case of $BW = 1$ GHz at 0 mK, indicated by the black curve, $g^{(2)}$ exhibits very strong bunching at $\tau = 0$. At a later delay $\tau \sim 15$ ns, $g^{(2)}$ for the transmitted field even appears antibunched [25]; this is, however, not resolved in the experimental data. For the other curves, we see the degrading of superbunching due to the influence of BW, temperature and jitter. In figure 9(c), we plot $g^{(2)}(0)$ as a function of incident power, and clearly see that the (super)bunching behavior decreases as the incident power increases. For high powers, where $\langle N_p \rangle \gg 1$, we find that $g^{(2)}(\tau) = 1$. This is because most of the coherent signal then passes through the transmission line without interacting with the qubit owing to saturation of the atomic response. We also plot the theoretical curves (blue) at 0 mK for two different BW.

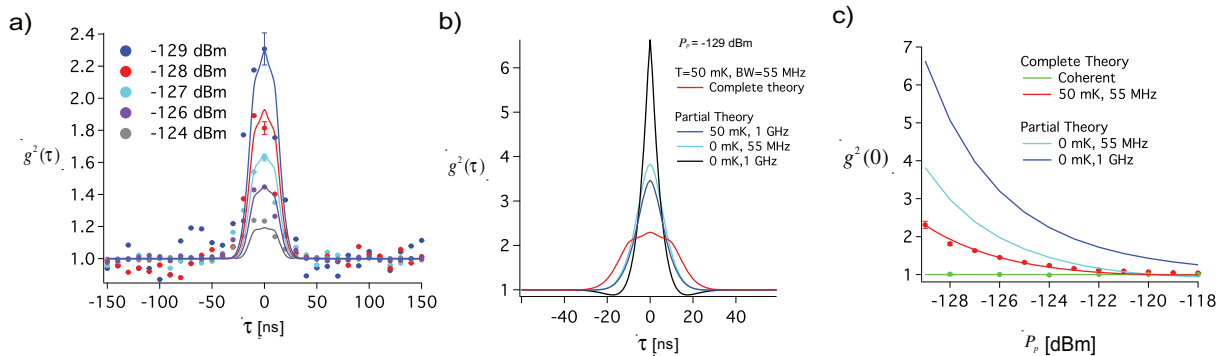


Figure 9. Second-order correlation function of the transmitted fields generated by the artificial atom (sample 2). (a) $g^{(2)}$ of the resonant transmitted microwaves as a function of delay time for five different incident powers. The peculiar feature of $g^{(2)}$ around zero in the theory curves is due to the trigger jitter model. (b) Influence of BW, temperature and jitter on superbunching. (c) $g^{(2)}(0)$ of the resonant transmitted field as a function of incident power. The result for a coherent state is also plotted. We see that the transmitted field statistics (red curve) approach those of a coherent field at high incident power, as expected. For $BW = 1$ GHz at 0 mK, we see very strong bunching at low incident power in the theory plot. The error bar indicated for each data (markers) set is the same for all the points. The solid curves in (a)–(c) are the theory curves. For all measurements shown here, we find that $g^{(2)}(\infty) = 1$, as expected.

A single-mode resonator is used to model the digital filter. The theoretical curves in figures 8 and 9 are based on a master equation describing both the transmon and the resonator using the formalism of cascaded quantum systems [33]. The trigger jitter is modeled by the following: the value of $g^{(2)}(\tau)$ at each point is replaced by the average value of $g^{(2)}(\tau - 10$ ns), $g^{(2)}(\tau)$ and $g^{(2)}(\tau + 10$ ns). We extract 50 mK from all these fits, with no additional free fitting parameters.

As we have shown, the single artificial atom acts as a photon-number filter, which selectively filters out the one-photon number state from a coherent state. This provides a novel way of generating single microwave photons [34–36].

5. Discussion

Microwave quantum optics with a single artificial atom opens up a novel way of building up a quantum network based on superconducting circuits. In such a system, superconducting processors can act as quantum nodes, which can be linked by quantum channels, to transfer flying photons (quantum information) from site to site on-chip with high fidelity. In this way, the single-photon router can switch quantum information on nanosecond timescales and with 99% efficiency, with the possibility of multiple outputs. The photon-number filter can act as the source of generation of flying microwave photons. These components have the advantage of a wide frequency range compared to cavity-based systems [35, 37, 38]. In addition, the recent development of a cross-Kerr phase shifter at the single-photon level based on superconducting circuits is also beneficial for a microwave quantum network [21].

While microwave quantum optics with artificial atoms is a promising technology for quantum information processing, optical photons have clear advantages for long-distance quantum communication via a quantum channel. The development of hybrid quantum networks would combine both advantages of these two systems. The early stages of optical–microwave interface have been demonstrated [39–41], with other potential coupling mechanisms under investigation [42–45].

6. Summary

Based on superconducting circuits, we study various fundamental quantum optical effects with a single artificial atom, for example photon scattering, Mollow triplet and Autler–Townes splitting. We further demonstrate two potential elements for an on-chip quantum network: the single-photon router and the photon-number filter.

Acknowledgments

We acknowledge financial support from the EU through the ERC and the project PROMISCE, from the Swedish Research Council and from the Wallenberg Foundation. B P acknowledges support from the CSIC grant JAE-PREDOC2009. We also acknowledge Thomas M Stace, Bixuan Fan, G J Milburn, Tim Duty and O Astafiev for fruitful discussions.

References

- [1] Schoelkopf R J and Girvin S M 2008 *Nature* **451** 664
- [2] Clarke J and Wilhelm F K 2008 *Nature* **453** 1031
- [3] Wendin G and Shumeiko V S 2007 *Low Temp. Phys.* **33** 724
- [4] Wallraff A, Schuster D I, Blais A, Frunzio L, Huang R S, Majer J, Kumar S, Girvin S M and Schoelkopf R J 2004 *Nature* **431** 162–7
- [5] Schuster D I *et al* 2007 *Nature* **445** 515–8
- [6] Hofheinz M *et al* 2009 *Nature* **459** 546–9
- [7] Reed M D, DiCarlo L, Nigg S E, Sun L, Frunzio L, Girvin S M and Schoelkopf R J 2012 *Nature* **482** 382
- [8] Fedorov A, Steffen L, Baur M, da Silva M P and Wallraff A 2012 *Nature* **481** 170–2
- [9] Vijay R, Macklin C, Slichter D H, Weber S J, Murch K W, Naik R, Korotkov A N and Siddiqi I 2012 *Nature* **490** 77
- [10] Mariani M *et al* 2011 *Science* **334** 61
- [11] Wilson C M, Johansson G, Pourkabirian A, Simoen M, Johansson J R, Duty T, Nori F and Delsing P 2011 *Nature* **479** 376–9
- [12] Castellanos-Beltran M A, Irwin K D, Hilton G C, Vale L R and Lehnert K W 2008 *Nature Phys.* **4** 929
- [13] Bergeal N, Schackert F, Metcalfe M, Vijayand R, Manucharyan V E, Frunzio L, Prober D E, Schoelkopf R J, Girvin S M and Devoret M H 2010 *Nature* **465** 64
- [14] Tey M K, Chen Z L, Aljunid S A, Chng B, Huber F, Maslennikov G and Kurtsiefer C 2008 *Nature Phys.* **4** 924–7
- [15] Hwang J, Pototschnig M, Lettow R, Zumofen G, Renn A, Gotzinger S and Sandoghdar V 2009 *Nature* **460** 76–80
- [16] Wrigge G, Gerhardt I, Hwang J, Zumofen G and Sandoghdar V 2008 *Nature Phys.* **4** 60–6
- [17] Gerhardt I, Wrigge G, Bushev P, Zumofen G, Agio M, Pfab R and Sandoghdar V 2007 *Phys. Rev. Lett.* **98** 033601

- [18] Astafiev O, Zagoskin A M, Abdumalikov A A, Pashkin Y A, Yamamoto T, Inomata K, Nakamura Y and Tsai J S 2010 *Science* **327** 840
- [19] Hoi I C, Wilson C, Johansson G, Palomaki T, Peropadre B and Delsing P 2011 *Phys. Rev. Lett.* **107** 073601
- [20] Hoi I C, Palomaki T, Johansson G, Lindkvist J, Delsing P and Wilson C M 2012 *Phys. Rev. Lett.* **108** 263601
- [21] Hoi I C, Wilson C M, Johansson G, Palomaki T, Stace T M, Fan B and Delsing P 2012 arXiv:1207.1203v1
- [22] Abdumalikov A A, Astafiev O, Zagoskin A M, Pashkin Y A, Nakamura Y and Tsai J S 2010 *Phys. Rev. Lett.* **104** 193601
- [23] Astafiev O V, Abdumalikov A A, Zagoskin A M, Pashkin Y A, Nakamura Y and Tsai J S 2010 *Phys. Rev. Lett.* **104** 183603
- [24] Shen J T and Fan S H 2005 *Phys. Rev. Lett.* **95** 213001
- [25] Chang D E, Sorensen A S, Demler E A and Lukin M D 2007 *Nature Phys.* **3** 807–12
- [26] Koch J, Yu T M, Gambetta J, Houck A A, Schuster D I, Majer J, Blais A, Devoret M H, Girvin S M and Schoelkopf R J 2007 *Phys. Rev. A* **76** 042319
- [27] Zumofen G, Mojarad N M, Sandoghdar V and Agio M 2008 *Phys. Rev. Lett.* **101** 180404
- [28] Mollow B R 1969 *Phys. Rev.* **188** 1969
- [29] Autler S H and Townes C H 1955 *Phys. Rev.* **100** 703–22
- [30] Zheng H, Gauthier D J and Baranger H U 2010 *Phys. Rev. A* **82** 063816
- [31] Brown R H and Twiss R Q 1956 *Nature* **177** 27–32
- [32] Loudon R 2000 *The Quantum Theory of Light* (Oxford: Oxford University Press)
- [33] Peropadre B, Lindkvist J, Hoi I C, Wilson C M, Garcia-Ripoll J, Delsing P and Johansson G 2012 arXiv:1210.2264v1
- [34] Mallet F, Castellanos-Beltran M A, Ku H S, Glancy S, Knill E, Irwin K D, Hilton G C, Vale L R and Lehnert K W 2011 *Phys. Rev. Lett.* **106** 220502
- [35] Bozyigit D *et al* 2011 *Nature Phys.* **7** 154
- [36] Wilson C M, Duty T, Sandberg M, Persson F, Shumeiko V and Delsing P 2010 *Phys. Rev. Lett.* **105** 233907
- [37] Rebic S, Twamley J and Milburn G J 2009 *Phys. Rev. Lett.* **103** 150503
- [38] Sandberg M, Persson F, Hoi I C, Wilson C M and Delsing P 2009 *Phys. Scr.* **T137** 014018
- [39] Kubo Y *et al* 2011 *Phys. Rev. Lett.* **107** 220501
- [40] Kubo Y *et al* 2010 *Phys. Rev. Lett.* **105** 140502
- [41] Staudt M U *et al* 2012 *J. Phys. B: At. Mol. Opt. Phys.* **45** 124019
- [42] Kielpinski D, Kafri D, Woolley M J, Milburn G J and Taylor J M 2012 *Phys. Rev. Lett.* **108** 130504
- [43] Wang Y D and Clerk A A 2012 *Phys. Rev. Lett.* **108** 153603
- [44] Kim Z *et al* 2011 *AIP Adv.* **1** 042107
- [45] Tian L 2012 *Phys. Rev. Lett.* **108** 153604